





Magnon transport and thermoelectric effects in ultrathin $\text{Tm}_3\text{Fe}_5\text{O}_{12}/\text{Pt}$ nonlocal devices

Jialiang Gao ^{1,*}, Charles-Henri Lambert,¹ Richard Schlitz ¹, Manfred Fiebig,²
Pietro Gambardella ¹ and Saül Vélez ^{1,2,3,†}

¹Laboratory for Magnetism and Interface Physics, Department of Materials, ETH Zurich, 8093 Zurich, Switzerland

²Laboratory for Multifunctional Ferromagnetic Materials, Department of Materials, ETH Zurich, 8093 Zurich, Switzerland

³Spintronics and Nanodevices Laboratory, Condensed Matter Physics Center (IFIMAC), Instituto Nicolás Cabrera, and Departamento de Física de la Materia Condensada, Universidad Autónoma de Madrid, E-28049 Madrid, Spain



(Received 26 January 2022; revised 17 October 2022; accepted 19 October 2022; published 26 December 2022)

The possibility of electrically exciting and detecting magnon currents in magnetic insulators has opened exciting perspectives for transporting spin information in electronic devices. However, the role of the magnetic field and the nonlocal thermal gradients on the magnon transport remain unclear. Here, by performing nonlocal harmonic voltage measurements, we investigate magnon transport in perpendicularly magnetized ultrathin $\text{Tm}_3\text{Fe}_5\text{O}_{12}$ (TmIG) films coupled to Pt electrodes. We show that the first harmonic nonlocal voltage captures spin-driven magnon transport in TmIG, as expected, and the second harmonic is dominated by thermoelectric voltages driven by current-induced thermal gradients at the detector. The magnon diffusion length in TmIG is found to be $\lambda_m \sim 0.3 \mu\text{m}$ at 0.5 T and gradually decays to $\lambda_m \sim 0.2 \mu\text{m}$ at 0.8 T, which we attribute to the suppression of the magnon relaxation time due to the increase of the Gilbert damping with field. By performing current-, magnetic field-, and distance-dependent nonlocal and local measurements we demonstrate that the second harmonic nonlocal voltage exhibits five thermoelectric contributions, which originate from the nonlocal spin Seebeck effect and the ordinary, planar, spin, and anomalous Nernst effects. Our work provides a guide on how to disentangle magnon signals from diverse thermoelectric voltages of spin and magnetic origin in nonlocal magnon devices, and establish the scaling laws of the thermoelectric voltages in metal/insulator bilayers.

DOI: [10.1103/PhysRevResearch.4.043214](https://doi.org/10.1103/PhysRevResearch.4.043214)

I. INTRODUCTION

Magnetic insulators (MI) coupled to heavy-metal (HM) layers are an ideal platform for the development of novel, yet highly efficient, spintronic devices [1–3]. For instance, the low magnetic moment and low Gilbert damping of thin-film ferrimagnetic garnets enable to stabilize chiral domain walls and electrically drive them with mobilities exceeding those attained with conventional ferromagnets [4–6]. Moreover, unlike in metals, magnon currents in MIs can propagate spin information over several micrometers, which can be electrically excited and detected by exploiting charge-to-spin conversion phenomena in HMs [7–9].

Magnon current injection and diffusion are typically investigated in MI/HM nonlocal device structures as the one shown in Fig. 1(a). The charge current injected in one HM stripe can drive magnon currents in the MI via both spin and heat transfer across the MI/HM interface (the charge

current generates both a spin current via the spin Hall effect (SHE) [10] and a thermal gradient via Joule heating; from now on, we will refer to these mechanisms as “electrical” and “thermal”, respectively), which are subsequently detected in a second nonlocal HM stripe by exploiting the reciprocal processes, i.e., the magnon-to-spin conversion at the MI/HM interface and the spin-to-charge conversion in the HM [8]. Magnon transport has been proven to be very efficient in low-damping materials such as $\text{Y}_3\text{Fe}_5\text{O}_{12}$ (YIG) [7,8,11–14] and $\alpha\text{-Fe}_2\text{O}_3$ [9,15,16]. However, several questions and challenges remain open. For instance, while earlier reports indicated that the magnon currents driven by electrical and thermal means should have the same propagation length [8,17], more recent works suggest they are different [14]. In addition, the generation of thermal magnon currents also results in nonlocal thermal gradients, which can lead to voltages of thermoelectric origin at the detector [18] and thus complicate the identification of the diffusive magnon currents. Besides, the influence of the external magnetic field on the transport characteristics of the magnon currents is not fully clear [14,19,20]. Yet, detailed magnon transport experiments have only been reported in a limited number of materials, typically involving relatively thick layers (>100 nm) of YIG. Therefore, it is essential that new materials with complementary properties are investigated. Furthermore, it is necessary to establish the scaling laws of the thermoelectric voltages in nonlocal devices to unambiguously disentangle diffusive magnon signals from spurious effects.

*Present address: Photonics Laboratory, Department of Information Technology and Electrical Engineering, ETH Zurich, 8093 Zurich, Switzerland.

†saul.velez@uam.es

Published by the American Physical Society under the terms of the [Creative Commons Attribution 4.0 International](https://creativecommons.org/licenses/by/4.0/) license. Further distribution of this work must maintain attribution to the author(s) and the published article's title, journal citation, and DOI.

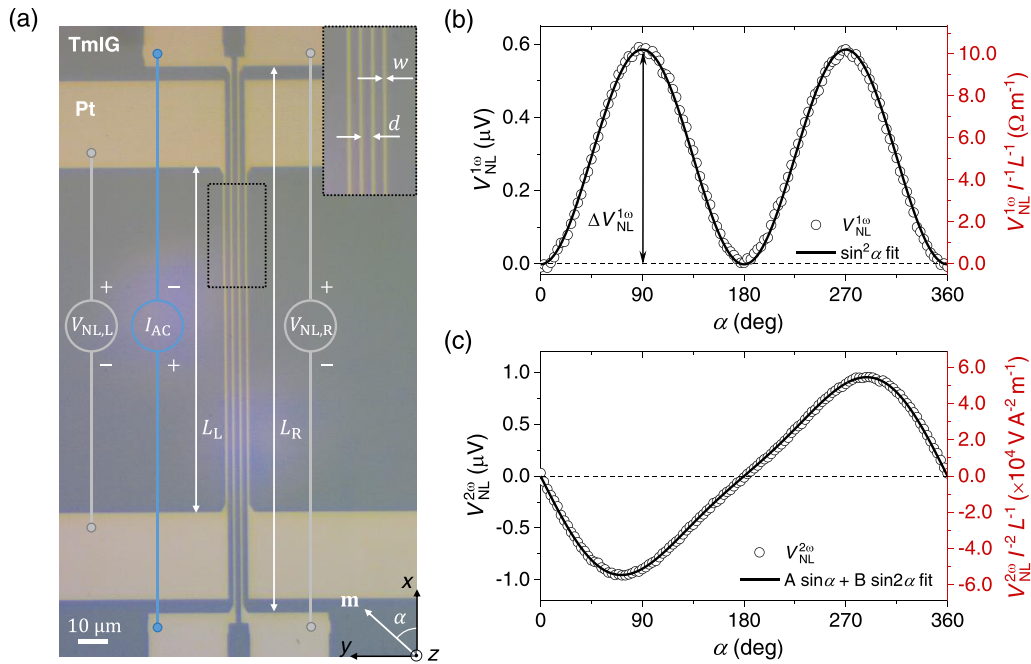


FIG. 1. (a) Optical image of a representative nonlocal device. The coordinate system, the rotation angle α , and the electric wiring employed in nonlocal measurements are indicated. The voltage in the current line is also measured as reference (not indicated for simplicity). The inset shows a zoom of the dashed area $w = 0.5 \mu\text{m}$, $d = 2.5 \mu\text{m}$, $L_R = 185 \mu\text{m}$, and $L_L = 125 \mu\text{m}$. (b), (c) Angular-dependent measurements of the first and second harmonic nonlocal voltage response $V_{\text{NL}}^{1\omega}$ and $V_{\text{NL}}^{2\omega}$ captured in the electrode located at the right-hand side of the current line for a device with $d = 1.2 \mu\text{m}$. The measurements are performed with an AC current excitation of amplitude $I = 310 \mu\text{A}$ and external field $B = 500 \text{ mT}$. The solid lines are fits to the experimental data. The right Y scale in (b) and (c) shows the $V_{\text{NL}}^{1\omega}$ and $V_{\text{NL}}^{2\omega}$ voltages normalized by the current (linear and quadratic, respectively) and length of the detector.

In this work, we report magnon transport experiments in sputter-grown perpendicularly magnetized ultrathin TmIG layers. By performing harmonic transport measurements in patterned nonlocal Pt devices, we can separate the signals arising from electrically generated magnon currents from those of thermal origin. The magnon diffusion length is determined by analyzing the exponential decay of the first harmonic signal for devices having different injector-detector distances. Moreover, we show that the external field leads to a reduction of the magnon diffusion length in TmIG due to the suppression of the magnon relaxation time with field. We explain the field dependence based on the Gilbert damping phenomenology and derive simple relations that describe the magnon transport in the presence of moderate magnetic fields. We also show that the thermally induced signals are captured in the second harmonic nonlocal response and are, however, dominated by the nonlocal thermal gradients induced nearby the detector rather than by diffusive magnon currents propagating from the injector. We identify five different thermoelectric contributions, namely, a nonlocal spin Seebeck effect (SSE) [18], an ordinary Nernst effect (ONE), a planar Nernst effect (PNE) [21], a spin Nernst effect (SNE) [22], and a thermoelectric anomalous Hall-like voltage originating from the anomalous Nernst effect (ANE) [23]. Finally, we show that by performing angular-, magnetic field-, and distance-dependent experiments it is possible to discern between thermal magnon currents and nonlocal SSE voltages [18], as well as to distinguish proximity-induced signals (such as the PNE and the ANE) from those

having same symmetry but spin origin (i.e., the SNE and the thermal spin drag (TSD) [24], respectively) in nonlocal devices.

II. EXPERIMENT DETAILS

A. Thin-film growth and characterization

The films were prepared by *in situ* sputter growth of TmIG and Pt. A 15-nm-thick TmIG layer was RF sputtered on Sc-substituted gadolinium gallium garnet single-crystal substrates ($\text{Gd}_3\text{Sc}_2\text{Ga}_3\text{O}_{12}$; GSGG) with a base pressure of 5×10^{-8} Torr. The growth temperature and the Ar pressure for the TmIG were 800°C and 0.2 Pa , respectively. After the deposition, the samples were annealed for 30 min at the deposition temperature and finally cooled back to room temperature in vacuum. In order to improve the TmIG/Pt interface quality, 4-nm Pt was DC sputtered at room temperature in the same chamber without breaking the vacuum. The Ar pressure during the Pt deposition was 0.4 Pa . The crystalline structure and topography of the layers were characterized by x-ray diffraction and atomic force microscopy measurements, the later revealing a root-mean-square roughness below 1 nm over a $5\text{-}\mu\text{m}^2$ surface area (see Appendix A for more details). The saturation magnetization of the 15-nm TmIG film investigated in this work was determined to be $M_s \sim 100 \text{ kA m}^{-1}$, which agrees with the reduction of M_s in films relative to the bulk value [4,25–27]. The anisotropy was characterized by spin Hall magnetoresistance (SMR) measurements in Hall bar devices [4,27–29], demonstrating that the film exhibits robust

perpendicular magnetic anisotropy with an anisotropy field ~ 400 mT and a coercive field $H_c \sim 30$ mT (see Appendix B).

B. Device fabrication

Hall bars and nonlocal devices having different distances between the Pt electrodes (center-to-center distances ranging from $d = 1.0$ to $4.1 \mu\text{m}$ and fixed width $w \sim 0.5 \mu\text{m}$) were patterned on the same film by high-resolution electron-beam lithography and Ar plasma etching. To that end, a 3-nm-thick Ti hard mask was patterned on the films by writing the structures on a polymethyl methacrylate layer, followed by the e-beam evaporation of Ti and lift-off. The final devices were produced by etching the uncovered Pt regions in low-power Ar^+ plasma, leaving the TmIG film unetched. Figure 1(a) shows an optical image of a representative nonlocal device with $d = 2.5 \mu\text{m}$. The long and short stripes have a length $L = 185$ and $125 \mu\text{m}$, respectively. (See Fig. 8(a) in Appendix B, which shows an optical image of a Hall bar device, which was used to perform local magnetotransport measurements.) Note that the Ti layer thickness was optimized to result in an ~ 1 -nm-thick nonconducting TiO_x capping layer on the Pt devices after etching.

C. Harmonic transport measurements

The transport measurements were performed in a room-temperature magnetotransport setup that allowed us to rotate the sample by 360° along any of the three main rotation axes of the devices. Harmonic transport measurements were performed by demodulating the detected voltage at integer multiples of the frequency of the injected alternating current (AC). This was realized by employing a sinusoidal current source synchronized with a multichannel high-frequency acquisition card module operating in continuous mode. A fast Fourier transformation of the voltage signals allows extracting the amplitude and phase of the different harmonics. This measurement scheme enables us to capture the voltage response of the device in multiple channels, which we employed to simultaneously record the local and nonlocal response of different Pt electrodes in nonlocal devices, as well as the longitudinal and transverse voltages in Hall bar structures. In the nonlocal measurements, the frequency of the injected current was fixed to 3 Hz to avoid spurious inductive signals. No current leakage through TmIG was detected in the current range employed in the experiments.

III. RESULTS AND DISCUSSION

A. Electrically and thermally induced nonlocal signals

The electrically and thermally induced signals can be decoupled by performing harmonic transport measurements. The first harmonic nonlocal response captures the signal arising from the electrical excitation of magnon currents (i.e., due to the charge-to-spin and the spin-to-magnon conversion), whereas the second harmonic proves the thermally driven magnons as well as thermoelectric signals arising from the thermal gradients induced at the detector [8]. An optical image of a representative nonlocal device investigated in this work is presented in Fig. 1(a).

Due to the symmetries of the effects involved in the excitation and detection of magnon currents, the nonlocal signals have characteristic angular dependences. Figures 1(b) and 1(c) show representative first and second harmonic nonlocal voltage measurements performed with a magnetic field \mathbf{B} rotating in the plane of the film. The strength of the magnetic field is selected to saturate the magnetization \mathbf{M} of TmIG along \mathbf{B} . The first harmonic response shows a $\sin^2\alpha$ dependence [α is the angle between the injected current and \mathbf{M} in the plane of the film; see Fig. 1(a)], reflecting the symmetry of the SHE and the inverse SHE at the injector and detector electrodes [8,14,17], respectively. Concretely, the spin-to-magnon excitation is maximal (zero) for \mathbf{M} collinear (perpendicular) to the spin accumulation μ_s at the TmIG/Pt interface, which is in the plane and perpendicular to the stripe, giving a $\sin\alpha$ dependence for magnon excitation at the injector. The second $\sin\alpha$ arises from the magnon-to-spin conversion at the detector, as the detection of the inverse SHE voltage is proportional to the alignment of \mathbf{M} in the direction perpendicular to the stripe. We thus confirm that the first harmonic signal in our TmIG/Pt nonlocal devices captures electrically driven diffusive magnons in TmIG.

The second harmonic signal has two contributions, one exhibiting a $\sin\alpha$ dependence and the other $\sin 2\alpha$ [see Fig. 1(c)]. The $\sin\alpha$ dependence is consistent with the detection of thermally driven magnon currents (which diffuse away from the injector region to the detector electrode and can be parametrized by the magnon chemical potential), as only the inverse SHE at the detector is involved [8,14,30]. However, the same symmetry is also observed for thermoelectric signals originated by vertical thermal gradients (i.e., perpendicular to the film plane) present at the detector region [18]. For thin MI layers, the vertical thermal gradient causes a magnon accumulation at the MI/substrate interface underneath the detector, resulting in a vertical diffusion and detection of magnons at the HM electrode. Because of its physical origin, we identify this thermoelectric signal as *non-local SSE*. Although both mechanisms result in signals having identical angular dependences, their origin stems from physical parameters having distinct decay lengths, i.e., the magnon chemical potential and the thermal diffusion, which decay exponentially and geometrically, respectively. Consequently, the thermal magnon currents can be distinguished from the nonlocal SSE by analyzing the decay of the signal with the injector-detector distance [14,18].

The $\sin 2\alpha$ contribution is consistent with a thermoelectric signal arising from the in-plane thermal gradient present at the detector electrode [22,24]. However, we note that in YIG/Pt nonlocal structures, the $\sin 2\alpha$ contribution was typically found to be negligible compared to the $\sin\alpha$ signal [8,14,22]. The origin of the different contributions to the second harmonic thermal signal in TmIG/Pt is analyzed in detail in Sec. III C. The distance and magnetic field dependences of the first harmonic, which include the analysis of the magnon diffusion length in TmIG, are presented in Sec. III B.

B. Electrically driven magnon currents

1. Determination of the magnon diffusion length

The magnon diffusion length can be extracted by measuring the decay of the first harmonic nonlocal signal with the

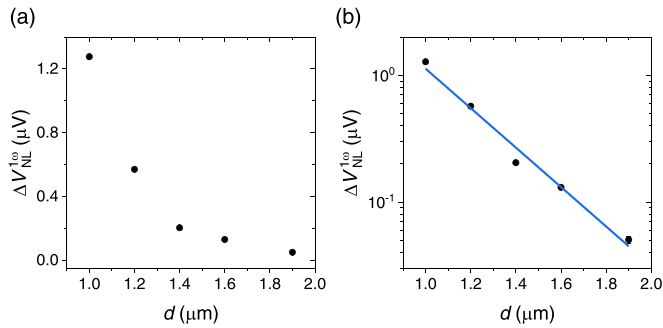


FIG. 2. (a) Amplitude of the first harmonic voltage $\Delta V_{\text{NL}}^{1\omega}$ measured for different injector-detector distances d . $B = 500$ mT, $L = 125 \mu\text{m}$, and $I = 310 \mu\text{A}$. The error bars are smaller than the size of the points. (b) Same data presented in (a) in logarithmic scale, showing that $\Delta V_{\text{NL}}^{1\omega}$ decays exponentially with d . The blue line is the fit of the data in the log scale to Eq. (1).

injector-detector distance d . Figure 2(a) shows the amplitude of the first harmonic signal $\Delta V_{\text{NL}}^{1\omega}$ [see Fig. 1(b)] measured in devices with different d and constant magnetic field. For diffusive magnons in the relaxation regime, i.e., for distances similar to or longer than the magnon diffusion length λ_m , and for film thicknesses $t < \lambda_m$, the nonlocal voltage decays with d as [8,17]

$$\Delta V_{\text{NL}}^{1\omega} = IL \frac{C}{\lambda_m} \exp\left(-\frac{d}{\lambda_m}\right), \quad (1)$$

where C is a distance-independent prefactor that depends on different parameters of the MI as well as the spin transmission efficiency across the HM/MI interface. Note that the length scale of magnon transport is characterized by a single parameter, here λ_m [Eq. (1)], regardless of the fact that magnons of different frequencies are driven by the electric current. This approximation, which is characteristic of diffusive transport, hinges on the efficient thermalization of magnons and phonons in the presence of weak spin nonconserving processes [17]. Such conditions are fulfilled in most magnon transport experiments. However, in extreme cases, such as in large damping materials, submillikelvin temperatures or very small injector-detector distances, the diffusive conditions may break down. In YIG, for instance, for distances below about $0.5 \mu\text{m}$ (i.e., $d \sim 0.05\lambda_m$), thermal magnons also contribute to the transport in contrast to the dominance of the subthermal magnons in the long-distance regime [31,32]. The dominant contribution of the subthermal magnons can be inferred, for instance, from the pronounced magnetic field dependence of λ_m [14,20]. This dependence originates from the field-induced relaxation of the low-frequency magnons, whereas the relaxation of the thermal magnons remains mostly unaffected by magnetic fields [33]. Besides, λ_m may depend on whether the magnons are driven electrically or thermally [14] or by large currents [34] as the result of the excitation of different nonequilibrium magnon distributions. In this work, we investigate magnon transport in TmIG in the linear diffusive regime, i.e., for relatively large injector-detector distances ($d \geq 1 \mu\text{m}$) and moderate driving currents and therefore expect the magnon transport to be dominated by subthermal magnons according to Eq. (1).

As demonstrated in Fig. 2(b), the signal decays exponentially with d in agreement with Eq. (1), from which we determine the magnon diffusion length of TmIG to be $\lambda_m(0.5 \text{ T}) = 0.28 \pm 0.02 \mu\text{m}$. This value is similar to the one indirectly estimated for TmIG via spin-wave spectroscopic measurements [35] but significantly lower than the magnon diffusion length measured in YIG thick films [8,11–14], $\alpha\text{-Fe}_2\text{O}_3$ [9,15], or NiFe_2O_4 [36,37]. The lower λ_m of TmIG can be explained by the larger damping α of this material ($\sim 10^{-2}$ [38,39]) compared to NiFe_2O_4 ($\sim 3.5 \times 10^{-3}$ [40]), $\alpha\text{-Fe}_2\text{O}_3$ ($\sim 10^{-4}$ [9,41]), and YIG ($\sim 10^{-4} - 10^{-5}$ even in thin films [42,43]). However, the magnon diffusion length in YIG films was found to decrease drastically upon reducing the film thickness [44,45], suggesting that not only the damping but also the scattering at the film surfaces may influence the magnon transport. In addition, we note that the magnon dispersion may be altered due to vertical confinement and thus influence the magnon manifold that contributes to the magnon transport. These questions, which go beyond the scope of this work, could be addressed via combined transport and spatially resolved Brillouin light-scattering experiments [34].

2. Field dependence of the magnon diffusion length

The magnon diffusion length in TmIG decays with magnetic field B , as evidenced by a steeper decrease of $\Delta V_{\text{NL}}^{1\omega}$ with d as B increases (Fig. 3). A reduction of λ_m with B has been observed in other MIs [9,14,19,20]. However, not only the field dependence of λ_m influences $\Delta V_{\text{NL}}^{1\omega}$, but also that of the prefactor $C(B)$ [19] [see Eq. (1)]. To investigate the role of B on the magnon transport characteristics, we measured the field dependence of $\Delta V_{\text{NL}}^{1\omega}$ by recording the nonlocal voltage while sweeping B in the plane of the film and perpendicular to the current line (i.e., parallel to μ_s). Figure 3(a) shows a representative $\Delta V_{\text{NL}}^{1\omega}(B)$ curve measured in a device with $d = 1.2 \mu\text{m}$. For fields below $|B| \sim 400$ mT [region indicated with a grayish-colored background in Fig. 3(a)], the magnetic field gradually tilts \mathbf{M} of TmIG towards the plane (see Appendix B), explaining the increase of the nonlocal signal as $|B|$ increases. A further increase of $|B|$, however, results in a suppression of the nonlocal signal. The same behavior with field is observed for different injector-detector distances [see Fig. 3(b), which presents $\Delta V_{\text{NL}}^{1\omega}(B)$ data for $B > 400$ mT; note that regardless of the field, the amplitude of the signal is smaller as d increases]. The decrease of $\Delta V_{\text{NL}}^{1\omega}$ with field was also observed in YIG as the result of the decrease of C and λ_m with B [19]. In the following we analyze the field dependence of these parameters in TmIG and discuss their origin.

$\lambda_m(B)$ and $C(B)$ can be obtained by fitting the decay of the nonlocal signal with d to Eq. (1) for different field values. Figures 3(c) and 3(d) show $\lambda_m(B)$ and $C(B)$ extracted from the data shown in Fig. 3(b) in the field range 450–800 mT. For $B > 800$ mT, the fits are not reliable due to the low signal-to-noise ratio in the devices with larger distances. λ_m gradually reduces with B from $\lambda_m = 0.29 \pm 0.01 \mu\text{m}$ at 450 mT to $\lambda_m = 0.23 \pm 0.02 \mu\text{m}$ at 800 mT. This corresponds to a relative change of λ_m of about 59% per Tesla field applied, which is about 35% larger than the one found for YIG in the same field range [19]. Although the uncertainty in the estimate of

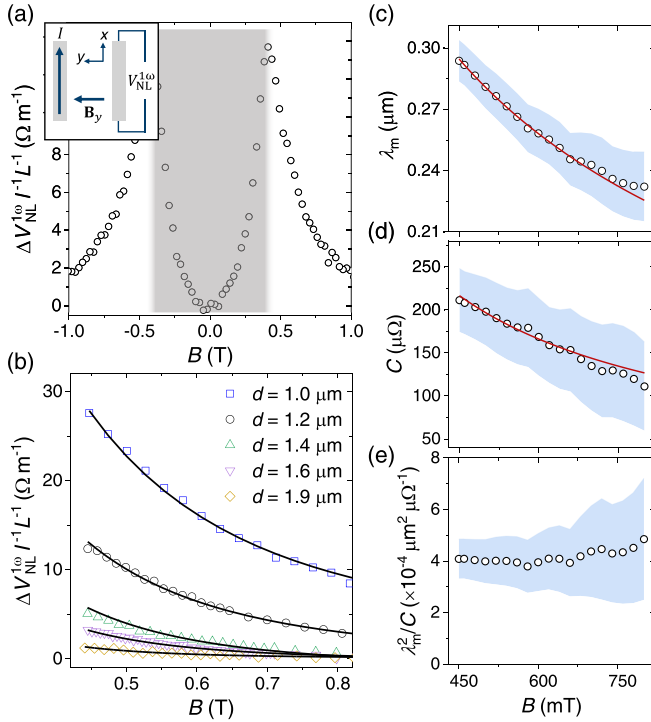


FIG. 3. (a) Field traces of $\Delta V_{NL}^{1\omega}$ measured for \mathbf{B} applied in the plane of the film and perpendicular to the current line. See inset for the measurement configuration. The gray-shaded area indicates the field region in which \mathbf{M} of TmIG is gradually aligning with \mathbf{B} (see Appendix B). $I = 310 \mu\text{A}$, $d = 1.2 \mu\text{m}$, and $L = 185 \mu\text{m}$. (b) $\Delta V_{NL}^{1\omega}(B)$ measured in devices with different injector-detector distances. Data shown for \mathbf{M} collinear to \mathbf{B} (open symbols). The injection current is $I = 310 \mu\text{A}$. The solid black lines are fits to the data by using Eq. (4). See text for details. (c), (d) Field dependence of λ_m and C extracted from fitting the data in (b) to Eq. (1) up to 800 mT (open symbols). Red solid lines in (c) and (d) are fits to the data points according to Eqs. (2) and (3), respectively. (e) λ_m^2/C computed from (c) and (d). The dashed blue area in (c), (d), and (e) represent half the standard deviation of the fitting and the corresponding error propagation.

$C(B)$ is large, the analysis shows that it also reduces with B [Fig. 3(d)].

To address the field dependence of λ_m and C , we need to consider that $\lambda_m = \sqrt{D_m \tau}$ and $C \propto D_m n$, where τ is the magnon relaxation time, D_m the magnon diffusion constant, and n the equilibrium magnon density [8]. Therefore, the magnetic field dependence of the magnon transport in TmIG could, in principle, be attributed to the field dependence of either τ , n , and D_m [19,46–48]. In fact, previous reports in YIG revealed that more than one transport parameter should influence the field dependence of the magnon diffusion [19], but it was not possible to identify which one was dominating, nor identify their field dependences. In the following, we will argue what field dependences are expected for τ , n , and D_m in the linear regime based on simple modeling and comparison with the magnon transport data in TmIG.

The magnetic field dependence of τ can be understood in the framework of the Gilbert damping phenomenology: the increase of the magnetic field increases the frequency

of the magnon modes, resulting in an enhancement of the magnon damping. In this context, it has been shown that the lifetime of the long-wavelength magnons, which are the ones that dominate the magnon transport [14,20], is given by $\tau(B) \approx \tau_0/(1 + \xi B)$ [33,49,50], where τ_0 is the magnon relaxation time at zero field, and ξ represents the enhancement of the magnon damping with field. By considering that $\lambda_m = \sqrt{D_m \tau}$, the field dependence of λ_m can be written as

$$\lambda_m \approx \frac{\lambda_{m,0}}{\sqrt{1 + \xi B}}, \quad (2)$$

where $\lambda_{m,0} = \sqrt{D_m \tau_0}$ is the magnon diffusion length at zero field and D_m a field-independent diffusion constant parameter. To find the field dependence of C , we computed $\frac{\lambda_m^2}{C} \propto \tau/n$ and found it to be fairly constant in the field range 450–800 mT [Fig. 3(e)], indicating that the magnon population decays with the magnetic field in a similar fashion as $\tau(B)$. Moreover, the slight upturn of τ/n in the range 700–800 mT suggests that $n(B)$ may decay slightly faster with field than $\tau(B)$, but the large uncertainty in the estimate of τ/n prevents us from inferring the exact field dependence of $n(B)$ in the high-field range. Assuming τ/n to be constant with field, the field dependence of C can be written as

$$C \approx \frac{C_0}{1 + \xi B}, \quad (3)$$

where $C_0 \propto n_0 D_m$ is the value of C at zero field with $n_0 = n(0)$. Using Eqs. (2) and (3), the field dependence of $\Delta V_{NL}^{1\omega}$ can be expressed as

$$\Delta V_{NL}^{1\omega}(B) \approx IL \frac{C_0}{\lambda_{m,0} \sqrt{1 + \xi B}} \exp\left(-\frac{d\sqrt{1 + \xi B}}{\lambda_{m,0}}\right). \quad (4)$$

By employing Eqs. (2)–(4) we obtain good fits to the experimental data with $\lambda_{m,0} = 0.98 \mu\text{m}$, $C_0 = 2412 \mu\Omega$, and $\xi = 22.5 \mu\text{T}^{-1}$ [see the black and red solid lines in Figs. 3(b)–3(d)]. Remarkably, the $\lambda_{m,0}$ and ξ values are in agreement with the larger magnon damping expected for TmIG compared to YIG, as $\lambda_{m,0} = 1.86 \mu\text{m}$ and $\xi = 0.83 \mu\text{T}^{-1}$ were found in YIG films of similar thickness [33].

Finally, we also want to point out that in the large-field regime the diffusion constant might be dependent on the magnetic field, $D_m(B)$, and that $\tau(B)$ may differ from the $(1 + \xi B)^{-1}$ dependence assumed above. This is because our relations are derived from a simplified Gilbert damping model that accounts for a linear with field increase of the damping, which is valid for the low-frequency magnons, and assumed a constant D_m . Moreover, the spin-mixing conductance at the Pt/TmIG interface, which we considered to be constant, could also influence the field dependence of C in the high-field range. Note that any of these deviations in the field dependences might also be the reason for the apparent increase of λ_m^2/C in the range from ~ 700 to 800 mT [Fig. 3(e)]. Nevertheless, we remark that our simple model [Eqs. (2)–(4)] captures very well the field trend of the experimental data presented in Figs. 3(b)–3(d). Future experimental and theoretical works should aim at investigating magnon diffusion in other MIs and its dependence at large fields, as well as address the origin of $\lambda_m(B)$, $n(B)$, and $D_m(B)$ from a microscopic perspective.

C. Nonlocal thermoelectric effects

In this section, we analyze the origin of the second harmonic signals. As shown in the schematic of Fig. 4(a), Joule dissipation at the injector electrode not only results in diffusive magnon currents propagating away from the injector/TmIG interface, but also in the build-up of thermal gradients at the detectors. As we will show, both thermal diffusive magnons and nonlocal thermal gradients contribute to the nonlocal second harmonic signal $V_{NL}^{2\omega}$, each having distinct angular, distance, and current dependences.

Figures 4(b) and 4(c) demonstrate that for an in-plane angular scan measurement, the $\sin\alpha$ contribution to $V_{NL}^{2\omega}$ has the same sign and amplitude (see blue curves) for detector stripes located at either side of the injector by the same distance. This is because the $\sin\alpha$ signal is linear with the vertical thermal gradient ∇T_z induced at the Pt-injector/MI interface, which generates diffusive magnon currents as well as ∇T_z gradients underneath the detectors, the latter resulting in nonlocal SSE-like signals [14,18]. Therefore, the ∇T_z contribution to $V_{NL}^{2\omega}$ is symmetric for detectors located at either side of the injector [see Fig. 4(a)]. The $\sin 2\alpha$ contribution, however, has the same amplitude but opposite sign for Pt stripes located at opposite sides of the injector [see Figs. 4(b) and 4(c), green curves], which strongly indicates that this signal is caused by the in-plane thermal gradient ∇T_y present at the detector. In addition to the linear dependence with the thermal gradients, note that the second harmonic voltages are also linear with the SHE at the detector, thus defining the sign of the signals. In the following, we analyze the distance dependence of the amplitude of these two contributions to $V_{NL}^{2\omega}$ and determine whether they originate from magnon or heat diffusion as well as whether the thermoelectric signals are of spin or magnetic nature. Last but not least, we also investigate a third thermoelectric contribution, which appears as an anomalous Hall-like response at the detector when sweeping the magnetic field perpendicular to the film plane.

1. Nonlocal spin Seebeck effect

The origin of the $\sin\alpha$ contribution to the second harmonic signal, which we label as $V_{NL-\nabla T_z}^{2\omega}$ [blue curves in Figs. 4(b) and 4(c)], can be determined by analyzing the decay of the signal with the injector-detector distance. Figure 5(a) shows the amplitude $V_{NL-\nabla T_z}^{2\omega}$ as function of d and for different magnetic fields. Unlike the case shown in Fig. 3 for $\Delta V_{NL}^{1\omega}$, $\Delta V_{NL-\nabla T_z}^{2\omega}$ is nearly field independent, suggesting that $V_{NL-\nabla T_z}^{2\omega}$ is originating from the nonlocal thermal gradients present nearby the detector rather than by diffusive magnons generated beneath the injector stripe. This interpretation is supported by the decay of the signal with d , which follows an $\sim 1/d^2$ dependence [see Fig. 5(b)] as expected for the radial spreading of heat from the injector to the TmIG/GSGG substrate [18,30] [due to the geometry of the electrodes, heat diffusion only occurs in the yz plane; see schematic of Fig. 4(a) and Fig. 10(a) in Appendix D, the later presenting the vertical thermal gradient ∇T_z computed at the TmIG/Pt-detector interface for different

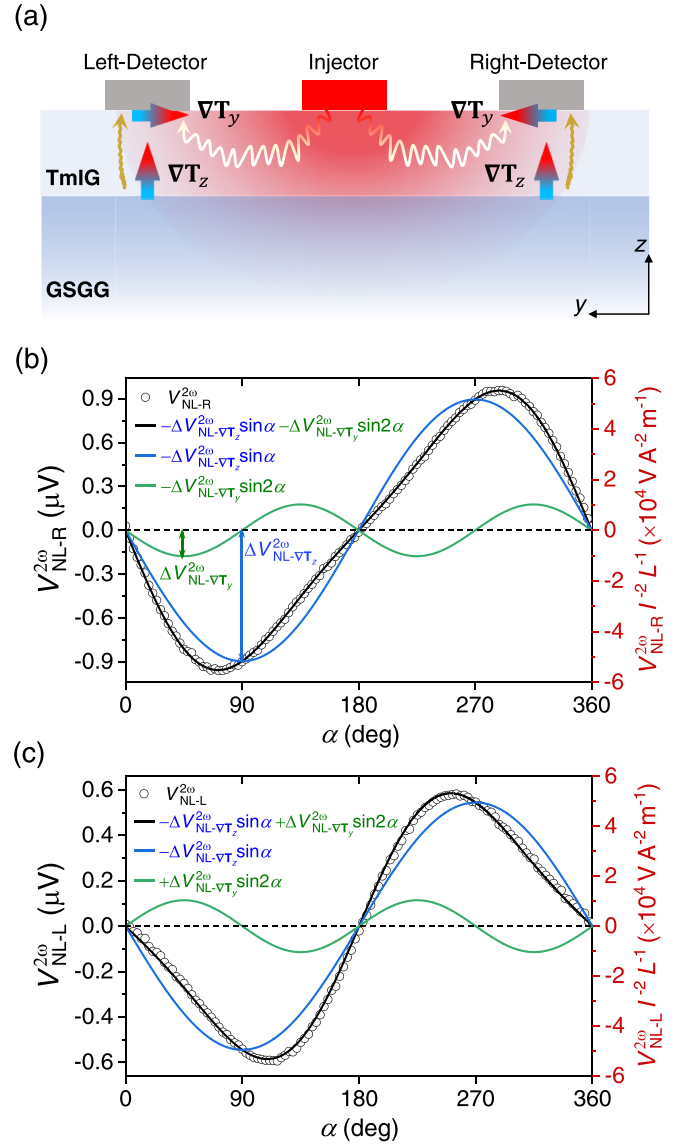


FIG. 4. (a) Cross-section schematic of the thermal gradients induced in the nonlocal devices. Magnon diffusion from the injector and from the GSGG/TmIG interface underneath the Pt detectors are schematically represented by wavy arrows. ∇T_z and ∇T_y indicate thermal gradients along the z and y directions, respectively. Note that the sketch is not to scale. (b), (c) In-plane angle scans of $V_{NL}^{2\omega}$ measured in detector electrodes located at the right- and left-hand side of the injector, respectively [see Fig. 1(a) for the measurement scheme]. Data taken in a device with $d = 1.2 \mu m$, $I = 310 \mu A$, and $B = 500 mT$. The scale at the right-hand side presents the voltage data normalized by the length of the detector ($L_R = 185 \mu m$, $L_L = 125 \mu m$) and the square of the current. The black lines are fits of the experimental data to an $A \sin \alpha + B \sin 2\alpha$ function. The $\sin \alpha$ contribution is the same for both detectors (blue curves), but the $\sin 2\alpha$ has the same amplitude but opposite sign between right and left detectors (green curves). These contributions are referred to in the text as $V_{NL-\nabla T_z}^{2\omega}$ and $V_{NL-\nabla T_y}^{2\omega}$, respectively. See (b) for the definition of the amplitudes and the text for details regarding the relative sign of the signals.

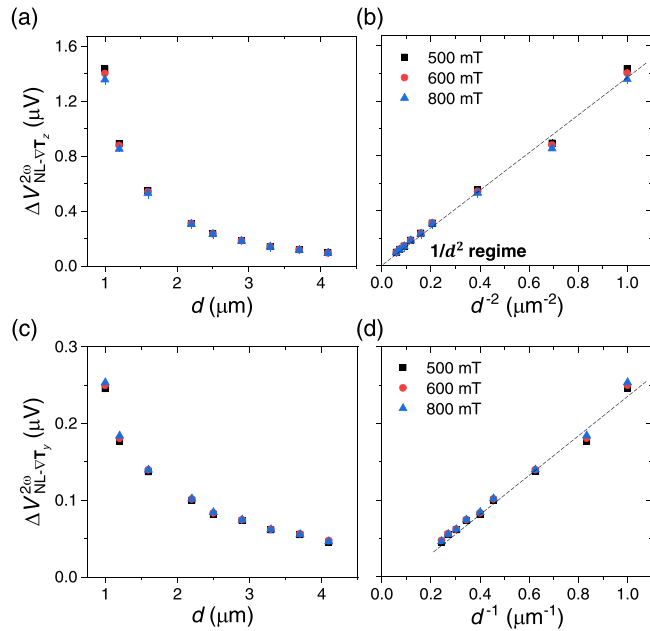


FIG. 5. (a) Amplitude of $V_{\text{NL}-\nabla T_z}^{2\omega}$ [blue curves in Figs. 4(b) and 4(c)] as function of the injector-detector distance and for different applied fields. The driving current is $I = 310 \mu\text{A}$. (b) Same data in (a) represented as $1/d^2$, demonstrating that $V_{\text{NL}-\nabla T_z}^{2\omega}$ decays geometrically with d (radially from the injector in the plane perpendicular to the current line), only exhibiting a slight deviation for the shortest injector-detector distances investigated ($d = 1.2$ and $1.0 \mu\text{m}$). The dashed line is a linear fit to the data with $d \geq 1.4 \mu\text{m}$ and extrapolated to large $1/d^2$ values. (c) Same as (a), but for the amplitude of $V_{\text{NL}-\nabla T_y}^{2\omega}$ [green curves in Figs. 4(b) and 4(c)]. (d) $\Delta V_{\text{NL}-\nabla T_y}^{2\omega}$ as function of $1/d$. The dashed line is a linear fit to the data. The data in (b) and (d) correlate with the decay with d of the thermal gradients $|\nabla T_z|$ and $|\nabla T_y|$, respectively, at the detector [see Fig. 10]. The length of the detector is $L = 185 \mu\text{m}$. The error in the data points is smaller than the size of the points.

d positions of the detector, demonstrating that ∇T_z indeed decays as $1/d^2$. Only for the shorter d values (1.0 and $1.2 \mu\text{m}$), the data slightly deviate from the $1/d^2$ dependence [dashed line in Fig. 5(b)], indicating that for these distances $V_{\text{NL}-\nabla T_z}^{2\omega}$ might start being influenced by the detection of diffusive magnons as well.

The $1/d^2$ dependence has also been observed in nonlocal Pt devices patterned on YIG films (micrometer-range thick) when d is larger than 3–5 times λ_m [14,18]. This crossover from the exponential to the $1/d^2$ regimes occurs when the thermal diffusion dominates over the diffusive magnon transport, as the latter decays much faster than the heat does (exponential vs radial decay). As a result, the nonlocal thermal gradient leads to a build-up magnon accumulation and diffusion from the MI/dielectric substrate interface. At the detector position, the vertical magnon diffusion results in a SSE-like signal and is thus commonly identified as *nonlocal SSE*. Given that in TmIG we could only explore devices with a minimal distance of $1 \mu\text{m}$ [~ 3 times λ_m according to first harmonic measurements; see Figs. 2(b) and 3(c)], it is reasonable that a dominant $\sim 1/d^2$ dependence is observed in our measurements, and expect that the thermal

diffusive magnon transport dominates $V_{\text{NL}-\nabla T_z}^{2\omega}$ for devices having shorter injector-detector distances.

We finally point out that if only a limited range of injector-detector distances is explored in materials with short λ_m [51,52], the exponential regime and the $1/d^2$ regime might be confused with each other. This calls for the need to investigate both the first and second harmonic signals to characterize diffusive magnon transport in MIs, as well as to explore $V_{\text{NL}-\nabla T_z}^{2\omega}$ for a wide range of d values to unambiguously identify the exponential regime associated with thermally driven magnon currents.

2. Planar spin Nernst effect

The $\sin 2\alpha$ thermoelectric contribution, which we label as $V_{\text{NL}-\nabla T_y}^{2\omega}$, reverses sign when inverting the position of the detector stripes [see green curves in Figs. 4(b) and 4(c)], indicating that it arises from the in-plane thermal gradient ∇T_y at the detector. This interpretation is supported by the fact that the amplitude of this signal does not depend on the magnetic field and decays as $1/d$ [see Figs. 5(c) and 5(d)], in agreement with the expected decay of $|\nabla T_y|$ with d [see Fig. 10(b) in Appendix D].

The $\sin 2\alpha$ dependence is consistent with the expected modulation by \mathbf{M} of TmIG of the thermally driven spin accumulation at the detector [22]. The physical mechanism is as follows. ∇T_y in Pt produces a transverse spin current by the SNE, which is further converted into a transverse charge current due to the inverse SHE. As a result, a thermally driven longitudinal voltage along ∇T_y is generated, an effect that is similar to the conventional Seebeck effect, but fundamentally different as it is driven by the spin-orbit coupling of the HM layer. Unlike the Seebeck effect, the heat-to-spin conversion induced by the SNE results in spin currents that can be modulated via the control of the spin transmission across the TmIG/Pt interface with \mathbf{M} . The control of the spin transmission leads to a modulation of the longitudinal thermoelectric signal ($|\nabla T_y$) as well as in a build-up transverse voltage, i.e., along the detector stripe, the latter having a $\sin 2\alpha$ angular dependence consistent with the experiment [green curves in Figs. 4(b) and 4(c)]. This effect can be regarded as the thermally driven counterpart of the transverse SMR.

We note that a thermoelectric signal with a $\sin 2\alpha$ dependence is also expected in metallic magnets in the presence of a transverse thermal gradient, an effect known as PNE [21]. Thus, the $V_{\text{NL}-\nabla T_y}^{2\omega}$ signal observed in the experiment could also be explained by the PNE at the detector if the Pt atoms at the interface with TmIG become magnetic due to the magnetic proximity effect (MPE) [53]. We investigated this possibility by performing local SMR measurements. The experiments revealed an anisotropic magnetoresistance (AMR) signal of about 10% of that of the SMR amplitude (see Appendix C), thus indicating that in our devices Pt exhibits a non-negligible MPE.

Unlike TmIG/Pt, in bulk YIG/Pt [8,11–14,29,54,55] as well as in other MPE-free MI/HM nonlocal magnon transport devices [36,37,51,52], $V_{\text{NL}-\nabla T_z}^{2\omega}$ was found to dominate the second harmonic signal. Experiments in ultrathin YIG(15 nm)/Pt films, however, revealed a significant $V_{\text{NL}-\nabla T_y}^{2\omega}$ contribution, which we attribute to the reduction of $V_{\text{NL}-\nabla T_z}^{2\omega}$ relative

to $V_{\text{NL}-\nabla T_y}^{2\omega}$ due to the decrease of the magnon diffusion length in YIG thin films [44]. Alternatively, in materials with longer λ_m values, $V_{\text{NL}-\nabla T_y}^{2\omega}$ should become relevant at sufficiently long injector-detector distances, but the decay of both signals with d makes it more difficult to be detected in the experiments. According to Ref. [22] and our estimation of the induced thermal gradients at the detector (Appendix D), we find that $\Delta V_{\text{NL}-\nabla T_y}^{2\omega}$ in our TmIG/Pt devices is about 50% larger than the one expected by the SNE. We thus conclude that both the SNE and the PNE, the latter driven by the MPE, contribute to $\Delta V_{\text{NL}-\nabla T_y}^{2\omega}$, and anticipate that thermoelectric signals driven by the SNE or the PNE will be more easily detected in materials with short magnon diffusion lengths.

Finally, we point out that for nonlocal second harmonic signals of purely thermoelectric origin (i.e., for $d \gg \lambda_m$; see Sec. III C 1), the contribution of $V_{\text{NL}-\nabla T_y}^{2\omega}$ relative to $\Delta V_{\text{NL}-\nabla T_z}^{2\omega}$ increases when increasing injector-detector distance. This is because $\Delta V_{\text{NL}-\nabla T_z}^{2\omega}$ decays as $1/d^2$, whereas $\Delta V_{\text{NL}-\nabla T_y}^{2\omega}$ decays as $1/d$. Therefore, the ratio $\Delta V_{\text{NL}-\nabla T_y}^{2\omega}/\Delta V_{\text{NL}-\nabla T_z}^{2\omega}$ will increase linearly with d , making the contribution of $V_{\text{NL}-\nabla T_y}^{2\omega}$ on $V_{\text{NL}}^{2\omega}$ more pronounced as d increases. In fact, in TmIG/Pt devices, it has been shown that for $d = 20 \mu\text{m}$, $\Delta V_{\text{NL}-\nabla T_y}^{2\omega}$ is already larger than $\Delta V_{\text{NL}-\nabla T_z}^{2\omega}$, and that for $d \sim 50 \mu\text{m}$, $\Delta V_{\text{NL}-\nabla T_z}^{2\omega}$ is negligible against $\Delta V_{\text{NL}-\nabla T_y}^{2\omega}$ [24].

3. Thermoelectric anomalous Hall-like signal

In the following, we will show that a third thermoelectric contribution, which arises from the in-plane thermal gradient ∇T_y and the MPE at the Pt detector, is detected in the nonlocal second harmonic response when the external magnetic field is swept perpendicular to the film.

Figure 6(a) shows a representative measurement of the nonlocal second harmonic voltage for \mathbf{B} swept along the out-of-plane direction (see inset schematics). The field trace reveals a thermoelectric anomalous Hall-like (TEAH) voltage $\Delta V_{\text{NL}-\text{TEAH}}^{2\omega}$ [see Fig. 6(a)] that correlates with the orientation of the magnetization of the TmIG layer [$\mathbf{M} = (0, 0, M_z)$] points out of the plane and switches at the field values at which $V_{\text{NL}-\text{TEAH}}^{2\omega}$ exhibits voltage jumps; see Appendix B]. A reversal of the position of the detector results in a reversal of $V_{\text{NL}-\text{TEAH}}^{2\omega}(B_z)$ [see Fig. 6(b)], indicating that this effect is linear with ∇T_y . In metallic ferromagnets, such signal response with B_z is attributed to the ANE. This scenario, however, changes with MIs as no electric conduction through the ferromagnet takes place. Similar TEAH signals have also recently been observed in MI/HM heterostructures and attributed to a different physical mechanism, a *thermal spin drag* [24] which originates from the combined action of ∇T_z and ∇T_y at the detector. According to the TSD, the out-of-plane thermal gradient ∇T_z at the MI/HM interface results in a spin current propagating along the z direction with the spin polarization pointing parallel to \mathbf{M} . The in-plane gradient ∇T_y in the HM then drags the spin current along its direction, which is detected as a thermoelectric voltage along the HM stripe due to the subsequent spin-to-charge conversion (note that the inverse SHE voltage is perpendicular to the spin polarization and the spin flow). Accordingly, the TSD is a

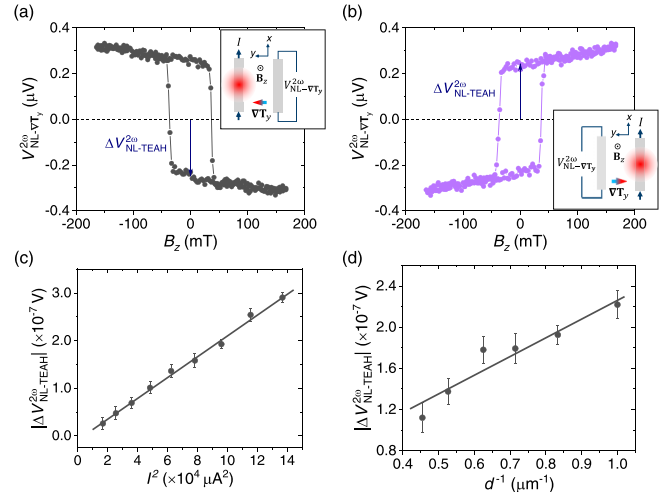


FIG. 6. (a), (b) Nonlocal second harmonic voltage measurements performed at detector electrodes located at the right- and left-hand side of the injector, respectively, while sweeping the magnetic field perpendicular to the plane. See inset schematics for the measurement configuration. The amplitude of the injected sinusoidal current is $I = 450 \mu\text{A}$, the injector-detector distance $d = 0.5 \mu\text{m}$, and $L_R = L_L = 125 \mu\text{m}$. The linear contribution with B_z is due to the ordinary Nernst effect in Pt, which is linear with ∇T_y as seen for the sign change between (a) and (b). Additionally, a thermoelectric anomalous Hall-like signal linear with the out-of-plane \mathbf{M} of TmIG and ∇T_y is observed. The amplitude and sign of this TEAH signal is indicated as $\Delta V_{\text{NL}-\text{TEAH}}^{2\omega}$. A device-dependent voltage offset is subtracted for clarity in (a) and (b). (c), (d) Current and distance dependence of $|\Delta V_{\text{NL}-\text{TEAH}}^{2\omega}|$ demonstrating that it follows a I^2 and $1/d$ dependence, respectively.

second-order thermoelectric effect and as such should have a current and distance dependence $\propto \nabla T_z \nabla T_y$. Given that any linear thermoelectric effect induced by either ∇T_z or ∇T_y , such as $\Delta V_{\text{NL}-\nabla T_z}^{2\omega}$ and $\Delta V_{\text{NL}-\nabla T_y}^{2\omega}$, is $\propto I^2$ (see Appendix E), and that ∇T_z and ∇T_y decay as $1/d^2$ and $1/d$ (see Fig. 10), respectively, we expect the TSD effect to be proportional to I^4 and decay as $1/d^3$.

Figures 6(c) and 6(d) show that $|\Delta V_{\text{NL}-\text{TEAH}}^{2\omega}|$ follows an $\sim I^2$ and a $\sim 1/d$ dependence, thus indicating that only ∇T_y contributes to the TEAH signal. We thus first consider whether $\Delta V_{\text{NL}-\text{TEAH}}^{2\omega}$ is originated by the SNE in Pt and M_z of TmIG through the imaginary component of the spin-mixing conductance G_i . This physical scenario is equivalent to the thermal counterpart of the anomalous Hall-like SMR signal due to G_i . Therefore, in an MPE-free system, the ratio $\frac{\Delta V_{\text{NL}-\text{TEAH}}^{2\omega}}{\Delta V_{\text{NL}-\nabla T_y}^{2\omega}}$ driven by the SNE should be comparable to the AHE-like/longitudinal SMR ratio. In our samples, however, we found the latter to be < 0.02 (see Fig. 8 for the data used for computation) while $\frac{\Delta V_{\text{NL}-\text{TEAH}}^{2\omega}}{\Delta V_{\text{NL}-\nabla T_y}^{2\omega}} \sim 0.57$, indicating that $\Delta V_{\text{NL}-\text{TEAH}}^{2\omega}$ cannot be driven solely by the SNE. Moreover, if only the SNE contribution to $\Delta V_{\text{NL}-\nabla T_y}^{2\omega}$ is considered, the ratio $\frac{\Delta V_{\text{NL}-\text{TEAH}}^{2\omega}}{\Delta V_{\text{NL}-\nabla T_y}^{2\omega}}$ exceeds 1. This is in contrast to measurements in MPE-free samples, where the AHE-like/longitudinal SMR ratio typically falls below 0.1 [56,57]. As described

in Sec. III C 2 and Appendix C, Pt in proximity with TmIG becomes partially magnetic. In this case, and for \mathbf{M} pointing out of the plane, an in-plane thermal gradient results in a $V_{\text{NL-TEAH}}^{2\omega}$ voltage due to the ANE in Pt [23]. We thus alternatively attribute the origin of the abnormally large $V_{\text{NL-TEAH}}^{2\omega}$ response in our sample to the anomalous Nernst effect driven by the MPE and $\nabla \mathbf{T}_y$ at the detector. Remarkably, the ratio ANE/PNE in ferromagnetic metals such as permalloy is similar to the one found in our system [58], further supporting the idea that $\Delta V_{\text{NL-TEAH}}^{2\omega}$ in our TmIG/Pt samples originates from magnetic moments induced in Pt by proximity with TmIG in contrast to the spin origin of the TSD.

We thus conclude that $V_{\text{NL-TEAH}}^{2\omega}$ in our devices is dominated by the MPE and $\nabla \mathbf{T}_y$ at the Pt detector. We remark that analyzing the current and distance dependence of $V_{\text{NL-TEAH}}^{2\omega}$ is a powerful tool for distinguishing between MPE-induced TEAH signals from those originated by the TSD effect. We also anticipate that the TSD effect might be better detected in the fourth harmonic response because the first-order (second harmonic) thermoelectric signals such as the ones originated by the MPE or G_i will be filtered out. We analyzed the fourth-harmonic nonlocal Hall voltage in our samples but could not identify any signal within the noise level. We expect that the methodology described here will guide future work aiming at clarifying the origin of thermally driven anomalous Hall-like signals in MI/HM bilayers.

IV. CONCLUSIONS

We have investigated magnon transport and nonlocal thermoelectric effects in perpendicularly magnetized ultrathin TmIG/Pt nonlocal devices. We have demonstrated the electrical detection of diffusive magnon spin signals to distances exceeding $1 \mu\text{m}$ and showed that Joule heating leads to a number of nonlocal thermoelectric effects. Remarkably, we have shown that by performing angle-, current-, and distance-dependent nonlocal and local harmonic transport measurements it is possible to distinguish between spin- and thermally driven magnon signals as well as to identify the origin of diverse thermoelectric voltages in MI/HM devices. In TmIG/Pt, we found that the out-of-plane thermal gradient at the TmIG/Pt-detector interface results in a nonlocal SSE, whereas the in-plane thermal gradient results in SNE, PNE, and ANE thermoelectric voltages. While the SNE is intrinsic of Pt, the PNE and the ANE emerge from the MPE at the TmIG/Pt interface. We also showed that nonlocal thermoelectric effects are more easy to be detected in devices exhibiting short magnon diffusion lengths (sub- μm range), and that the SNE, PNE, and ANE will eventually dominate over the nonlocal SSE in the long-distance regime. We finally discussed how to distinguish between the TSD and the ANE and concluded that in our devices the TSD is negligible. A table summarizing the amplitude of each thermoelectric contribution to the second harmonic signal is given in Appendix F. It is worth noting that the thermoelectric effects investigated here are not exclusive to magnon transport devices but expected to be present in any MI/HM heterostructure whenever thermal gradients are present.

We furthermore showed that the magnon diffusion length λ_m and the distance-independent scaling prefactor of the non-

local signal C in TmIG decrease with the magnetic field, which we attribute to the suppression of τ and n with increasing magnetic field. We derived simple relations for $\tau(B)$, $n(B)$, $\lambda_m(B)$, and $C(B)$ based on a linear increase of the Gilbert damping with field and comparison with the experimental data, and showed that they can nicely reproduce $V_{\text{NL}}^{1\omega}(B, d)$ in the field range explored. Future work should aim at addressing the microscopic origin of the field dependence of the magnon transport, as well as determine whether other parameters such as D_m also contribute to the magnetic field dependence.

Finally, our work further validates sputter growth as a suitable deposition technique to fabricate thin-film oxides and oxide/metal bilayers for spintronic applications. The possibility of combining magnon transport with other device functionalities such as current-induced switching and domain wall motion in perpendicularly magnetized layers coupled to HMs open prospects for developing novel device concepts.

ACKNOWLEDGMENTS

This project has received support by the Swiss National Science Foundation (SNSF) via Projects No. 198642, No. 200020-172775, and No. 200021-178825, by the European Research Council through the Advanced Grant No. 694955-INSEETO, by the ETH Zurich through the Career Seed Grant No. SEED-20 19-2. S.V. acknowledges support by the Spanish Ministry of Science and Innovation via Grant No. PID2021-122980OA-C53 and by the Comunidad de Madrid through the Atracción de Talento Grant No. 2020-T1/IND20041. J.G. acknowledges support from the IDEA scholarship and the Zeno Karl Schindler Foundation.

APPENDIX A: CRYSTALLOGRAPHIC AND TOPOGRAPHIC CHARACTERIZATION OF THE TmIG FILMS

Figure 7 presents the crystallographic and topographic characterization of the TmIG films.

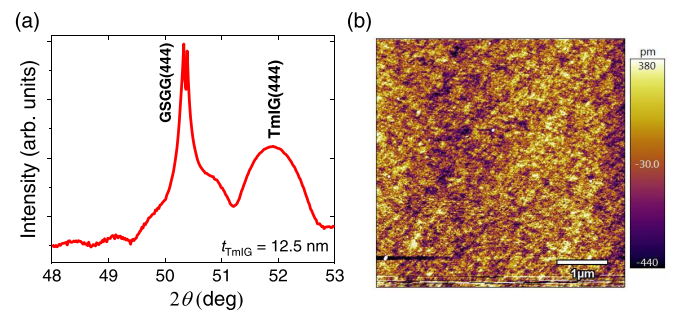


FIG. 7. (a) Structural characterization of a representative TmIG (12.5 nm) thin film. The $2\theta-\omega$ x-ray diffraction scan around the (444) peak of TmIG reveals a Laue diffraction peak and Laue oscillations characteristic of fully strained epitaxial films [4,27]. (b) Surface topographic characterization of a representative TmIG (30-nm) film via atomic force microscopy. The root-mean-square roughness is less than 1 nm over a $5 \times 5\text{-}\mu\text{m}^2$ surface area. Films with a Pt (4-nm) top layer exhibit the same roughness.

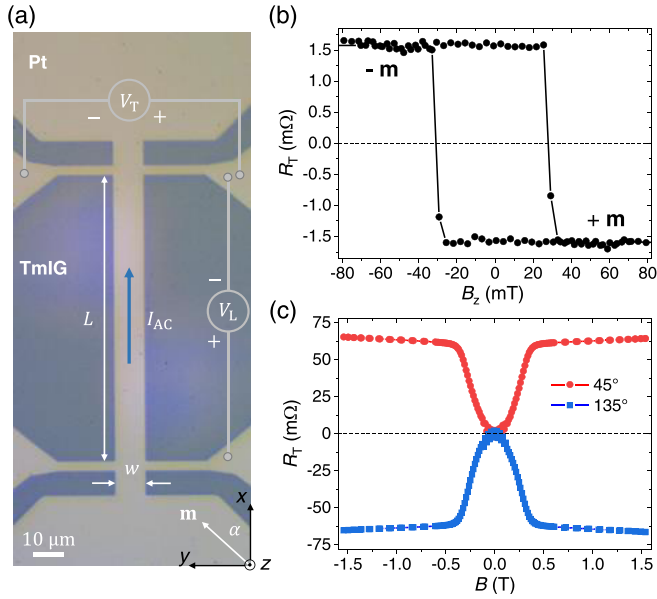


FIG. 8. (a) Optical image of a Pt Hall bar patterned on the 15-nm-thick TmIG film investigated in this work. The electric wiring employed in the measurements, the coordinate system, and the direction of field rotation are indicated. (b) Transverse magnetoresistance measurement $R_T = V_T/I$ performed while sweeping the out-of-plane field B_z . The coercive field is $H_c \sim 30$ mT. (c) Transverse magnetoresistance measurements performed with a magnetic field applied in the plane of the film and at an angle $\alpha = 45^\circ$ (red solid dots) and 135° (blue solid dots) from the current line. See panel (a) for the definition of α . The graph contains both the trace and retrace curves. From these measurements, we determine the anisotropy field to be ~ 400 mT.

APPENDIX B: ELECTRIC CHARACTERIZATION OF THE MAGNETIC ANISOTROPY AND THE COERCIVE FIELD OF TMIG

The magnetic anisotropy of TmIG films can be characterized by SMR measurements [4,27–29]. Figure 8(a) shows an optical image of a Pt Hall bar patterned on the TmIG (15-nm) film. The electric wiring employed in the local transport measurements is indicated. Figure 8(b) shows a transverse magnetoresistance measurement while sweeping the out-of-plane field B_z . The measurement reveals a clear square-shaped anomalous Hall-like response, demonstrating that the films exhibit robust perpendicular magnetic anisotropy with a coercive field $H_c \sim 30$ mT. Figure 8(c) shows the transverse magnetoresistance measured for \mathbf{B} applied in the plane of the film and at an angle $\alpha = 45^\circ$ and 135° from the current line (red and blue solid dots, respectively). The gradual change of resistance from $B = 0$ to ~ 400 mT is due to the gradual tilt of \mathbf{M} of TmIG towards \mathbf{B} , thus indicating that the anisotropy field of TmIG is ~ 400 mT. Note that the signals at 45° and 135° have same amplitude but opposite sign due to the $\sin 2\alpha$ symmetry of the transverse SMR.

APPENDIX C: LONGITUDINAL SMR MEASUREMENTS—MPE IN PT ON TMIG

The MPE in Pt can be identified from longitudinal SMR measurements [29]. Figure 9 shows angular-dependent longi-

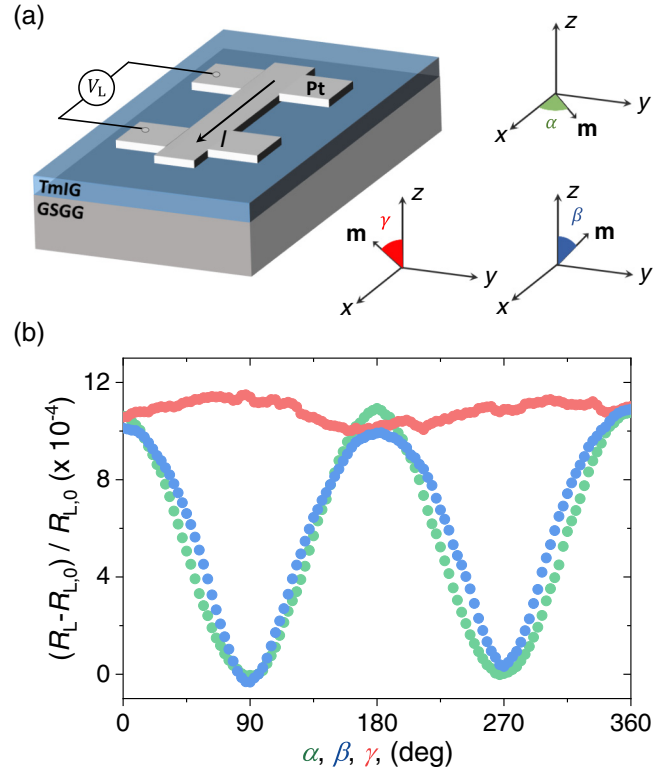


FIG. 9. (a), (b) Longitudinal spin Hall magnetoresistance performed along the three main axes of the device. See sketch in (a) for the definition of the angles, the color code of the measurement plane, and the coordinate system. An optical image of the device and the measurement scheme employed is shown in Fig. 8(a). The SMR amplitude is defined as $\Delta R_L = \frac{R_L - R_{L,0}}{R_{L,0}}$, where $R_L = V_L/I$ and $R_{L,0} = R_L(\mathbf{B}||\mathbf{y})$. The amplitude of the magnetoresistance in the xz plane is $\sim 10\%$ of that measured in the xy plane. We ruled out that this signal arises from a misalignment of the sample with the field. We thus conclude that TmIG induces a magnetic moment in Pt due to proximity at the interface.

tudinal SMR measurements performed along the three main axes of the device. According to SMR, the magnetoresistance modulation along the xy and yz planes should be identical, and no magnetoresistance should be visible in the xz plane [29,59] [see sketches in Fig. 9(a) for the definition of the rotation planes]. However, a magnetoresistance amplitude $\sim 10\%$ of that observed in the xy plane is detected in the xz plane, which indicates the presence of a finite AMR. We rule out that this signal arises from ordinary magnetoresistance in Pt films as the resistivity in our devices is $\sim 45 \mu\Omega \text{ cm}$ (a resistivity of about $20 \mu\Omega \text{ cm}$ would be necessary [60,61]). The presence of AMR thus indicates that the Pt atoms in proximity with TmIG become magnetic. The presence of MPE at MI/HM interfaces has been a topic of intense debate in the last decade [3,28,53,57,62–65], now accepted to be strongly dependent on the materials involved and the deposition conditions. In TmIG/Pt, previous magnetotransport studies did not report clear evidence of MPE [4,5,24–27], but a surprisingly large spin-mixing conductance as well as a large induced magnetic moment per Pt atom at the interface with TmIG were estimated from magnetometry measurements [4]. It is therefore

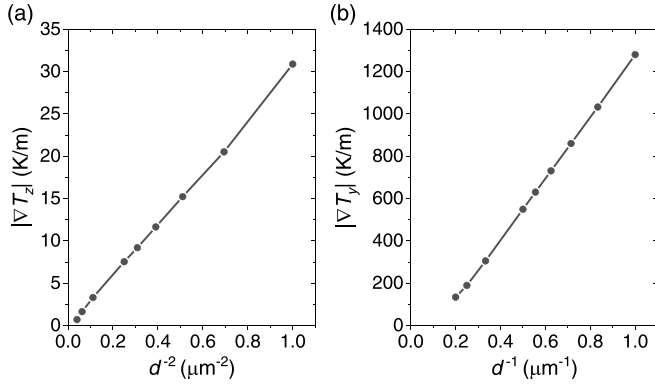


FIG. 10. (a) Average out-of-plane thermal gradient $|\nabla T_z|$ underneath the detector as function of $1/d^2$. (b) Average in-plane thermal gradient $|\nabla T_y|$ at the detector as function of $1/d$. Here we consider a heat power dissipation of 1.5 mW at the injector. See text for more details regarding the simulations.

plausible that in our devices the MPE at the TmIG/Pt interface induces a magnetic moment in Pt.

APPENDIX D: COMPUTATION OF ∇T_z AND ∇T_x AT THE DETECTOR

By employing a finite-element analysis simulation (Partial Differential Equation ToolboxTM in MATLAB), we compute the thermal gradients $|\nabla T_z|$ and $|\nabla T_y|$ at the detector position. Because of the symmetry of the system, only thermal diffusion in the yz plane is taken into account. For the simulation, we considered the current injector as a heat source and compute the thermal gradients ∇T_z and ∇T_y at different positions across the heterostructure [Fig. 4(a) shows a schematic of the device layout; note that the thickness of TmIG is not represented at scale]. In the simulation, we considered the dimensions of the electrodes as the ones employed in the experiment, and the thermal conductivities of TmIG/GSGG

TABLE I. Amplitude of the different thermoelectric contributions to $V_{NL}^{2\omega}$ in TmIG/Pt for representative injector-detector distances. $\Delta V_{NL-\nabla T_z}^{2\omega}$ and $\Delta V_{NL-\nabla T_y}^{2\omega}$ are extracted from measurements at 500 mT. These two thermoelectric contributions are nearly field independent in the field range investigated (Fig. 5). All voltage components are normalized by $I^2 L$. All amplitudes are given in units of $\times 10^4 \text{ VA}^{-2} \text{ m}^{-1}$. No data for $\Delta V_{NL-\text{TEAH}}^{2\omega}$ at $d = 3.3 \text{ } \mu\text{m}$ is available.

	$\Delta V_{NL-\nabla T_z}^{2\omega}$	$\Delta V_{NL-\nabla T_y}^{2\omega}$	$\Delta V_{NL-\text{TEAH}}^{2\omega}$
$d = 1.2 \text{ } \mu\text{m}$	5.2	1.0	1.6
$d = 2.2 \text{ } \mu\text{m}$	1.8	0.58	0.95
$d = 3.3 \text{ } \mu\text{m}$	0.82	0.35	

and Pt to be 8 and 26 W/mK, respectively [30]. The thickness of the GSGG substrate was considered semi-infinite as it is larger than the lateral dimensions of the experiment. We consider the current line to dissipate heat at an average rate of 1.5 mW, which corresponds to the power dissipation of an AC current of amplitude $I = 310 \text{ } \mu\text{A}$ at the injector electrode, a characteristic value employed in the experiments. ∇T_z and ∇T_y are computed as the average of the out-of-plane and in-plane thermal gradient values in TmIG and Pt, respectively, at the region covered by the detector electrode. Figures 10(a) and 10(b) show the computed $|\nabla T_z|$ and $|\nabla T_y|$, showing that they decay with the injector-detector distance as $1/d^2$ and $1/d$, respectively.

APPENDIX E: CURRENT DEPENDENCE OF $V_{NL}^{1\omega}$, $V_{NL-\nabla T_z}^{2\omega}$, AND $V_{NL-\nabla T_y}^{2\omega}$

The first and second harmonic nonlocal voltage response are odd and even with the AC current excitation, respectively [8]. Therefore, at the lowest order, they are linear and quadratic with I . Figure 11(a) shows the current dependence of $\Delta V_{NL}^{1\omega}$ demonstrating that it is linear with I . Figures 11(b) and 11(c) show the current dependence of $\Delta V_{NL-\nabla T_z}^{2\omega}$ and

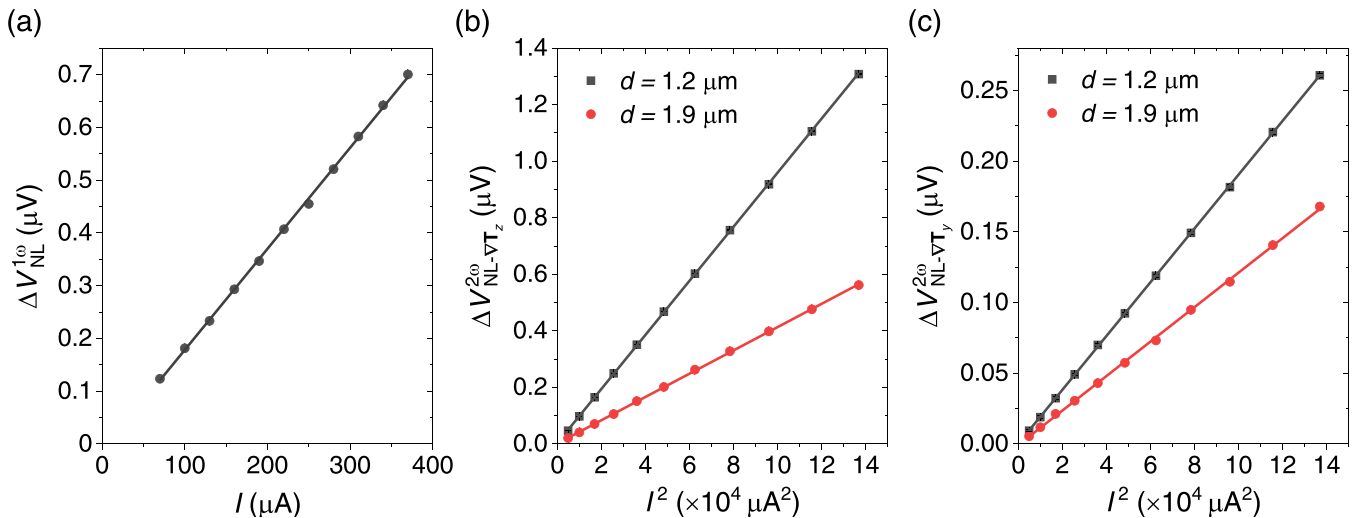


FIG. 11. (a) First harmonic nonlocal voltage measured as function of the AC current I . Data taken in a device with $d = 1.2 \text{ } \mu\text{m}$ and $L = 185 \text{ } \mu\text{m}$. (b), (c) $\Delta V_{NL-\nabla T_z}^{2\omega}$ and $\Delta V_{NL-\nabla T_y}^{2\omega}$, respectively, as function of I^2 measured in devices with different injector-detector distances and fixed detector length $L = 185 \text{ } \mu\text{m}$. $B = 500 \text{ mT}$ in all measurements.

$\Delta V_{\text{NL}-\nabla T_y}^{2\omega}$ for devices having different injector-detector distances, demonstrating that the signals are proportional to I^2 as expected.

APPENDIX F: AMPLITUDE OF THE DIFFERENT THERMOELECTRIC CONTRIBUTIONS

Table I summarizes the amplitude of the different thermoelectric contributions to the second harmonic signal in our

TmIG/Pt nonlocal devices. $\Delta V_{\text{NL}-\nabla T_z}^{2\omega}$ is dominated by the nonlocal SSE with negligible magnon-transport contribution (Sec. III C 1). $\Delta V_{\text{NL}-\nabla T_y}^{2\omega}$ stands for both SNE- and MPE-induced PNE at the Pt detector. According to our estimates of the SNE in Pt, we conclude that both SNE and PNE contribute to $\Delta V_{\text{NL}-\nabla T_y}^{2\omega}$ with a similar amplitude in our TmIG/Pt devices (Sec. III C 2). $\Delta V_{\text{NL}-\text{TEAH}}^{2\omega}$ is dominated by the MPE-induced ANE at the Pt detector with negligible TSD signal (Sec. III C 3).

-
- [1] A. V. Chumak, V. I. Vasyuchka, A. A. Serga, and B. Hillebrands, Magnon spintronics, *Nat. Phys.* **11**, 453 (2015).
- [2] V. E. Demidov, S. Urazhdin, G. de Loubens, O. Klein, V. Cros, A. Anane, and S. O. Demokritov, Magnetization oscillations and waves driven by pure spin currents, *Phys. Rep.* **673**, 1 (2017).
- [3] M. Althammer, Pure spin currents in magnetically ordered insulator/normal metal heterostructures, *J. Phys. D: Appl. Phys.* **51**, 313001 (2018).
- [4] S. Vélez, J. Schaab, M. S. S. Wörnle, M. Müller, E. Gradauskaitė, P. Welter, C. Gutgsell, C. Nistor, C. L. L. Degen, M. Trassin, M. Fiebig, and P. Gambardella, High-speed domain wall racetracks in a magnetic insulator, *Nat. Commun.* **10**, 4750 (2019).
- [5] C. O. Avci, E. Rosenberg, L. Caretta, F. Büttner, M. Mann, C. Marcus, D. Bono, C. A. Ross, and G. S. D. Beach, Interface-driven chiral magnetism and current-driven domain walls in insulating magnetic garnets, *Nat. Nanotechnol.* **14**, 561 (2019).
- [6] L. Caretta, S.-H. Oh, T. Fakhru, D.-K. Lee, B. H. Lee, S. K. Kim, C. A. Ross, K.-J. Lee, and G. S. D. Beach, Relativistic kinematics of a magnetic soliton, *Science* **370**, 1438 (2020).
- [7] Y. Kajiwara, K. Harii, S. Takahashi, J. Ohe, K. Uchida, M. Mizuguchi, H. Umezawa, H. Kawai, K. Ando, K. Takanashi, S. Maekawa, and E. Saitoh, Transmission of electrical signals by spin-wave interconversion in a magnetic insulator, *Nature (London)* **464**, 262 (2010).
- [8] L. J. Cornelissen, J. Liu, R. A. Duine, J. Ben Youssef, and B. J. van Wees, Long-distance transport of magnon spin information in a magnetic insulator at room temperature, *Nat. Phys.* **11**, 1022 (2015).
- [9] R. Lebrun, A. Ross, S. A. Bender, A. Qaiumzadeh, L. Baldrati, J. Cramer, A. Brataas, R. A. Duine, and M. Kläui, Tunable long-distance spin transport in a crystalline antiferromagnetic iron oxide, *Nature (London)* **561**, 222 (2018).
- [10] J. Sinova, S. O. Valenzuela, J. Wunderlich, C. H. Back, and T. Jungwirth, Spin Hall effects, *Rev. Mod. Phys.* **87**, 1213 (2015).
- [11] L. J. Cornelissen, J. Shan, and B. J. van Wees, Temperature dependence of the magnon spin diffusion length and magnon spin conductivity in the magnetic insulator yttrium iron garnet, *Phys. Rev. B* **94**, 180402(R) (2016).
- [12] B. L. Giles, Z. Yang, J. S. Jamison, and R. C. Myers, Long range pure magnon spin diffusion observed in a non-local spin-Seebeck geometry, *Phys. Rev. B* **92**, 224415 (2015).
- [13] B. L. Giles, Z. Yang, J. S. Jamison, J. M. Gomez-Perez, S. Vélez, L. E. Hueso, F. Casanova, and R. C. Myers, Thermally driven long-range magnon spin currents in yttrium iron garnet due to intrinsic spin Seebeck effect, *Phys. Rev. B* **96**, 180412(R) (2017).
- [14] J. M. Gomez-Perez, S. Vélez, L. E. Hueso, and F. Casanova, Differences in the magnon diffusion length for electrically and thermally driven magnon currents in $\text{Y}_3\text{Fe}_5\text{O}_{12}$, *Phys. Rev. B* **101**, 184420 (2020).
- [15] A. Ross, R. Lebrun, O. Gomonay, D. A. Grave, A. Kay, L. Baldrati, S. Becker, A. Qaiumzadeh, C. Ulloa, G. Jakob, F. Kronast, J. Sinova, R. Duine, A. Brataas, A. Rothschild, and M. Kläui, Propagation length of antiferromagnetic magnons governed by domain configurations, *Nano Lett.* **20**, 306 (2020).
- [16] T. Wimmer, A. Kamra, J. Gückelhorn, M. Opel, S. Geprägs, R. Gross, H. Huebl, and M. Althammer, Observation of Antiferromagnetic Magnon Pseudospin Dynamics and the Hanle Effect, *Phys. Rev. Lett.* **125**, 247204 (2020).
- [17] L. J. Cornelissen, K. J. H. Peters, G. E. W. Bauer, R. A. Duine, and B. J. Van Wees, Magnon spin transport driven by the magnon chemical potential in a magnetic insulator, *Phys. Rev. B* **94**, 014412 (2016).
- [18] J. Shan, L. J. Cornelissen, J. Liu, J. Ben Youssef, L. Liang, and B. J. Van Wees, Criteria for accurate determination of the magnon relaxation length from the nonlocal spin Seebeck effect, *Phys. Rev. B* **96**, 184427 (2017).
- [19] L. J. Cornelissen and B. J. van Wees, Magnetic field dependence of the magnon spin diffusion length in the magnetic insulator yttrium iron garnet, *Phys. Rev. B* **93**, 020403(R) (2016).
- [20] K. Oyanagi, T. Kikkawa, and E. Saitoh, Magnetic field dependence of the nonlocal spin Seebeck effect in Pt/YIG/Pt systems at low temperatures, *AIP Adv.* **10**, 015031 (2020).
- [21] A. D. Avery, M. R. Pufall, and B. L. Zink, Observation of the Planar Nernst Effect in Permalloy and Nickel Thin Films with In-Plane Thermal Gradients, *Phys. Rev. Lett.* **109**, 196602 (2012).
- [22] S. Meyer, Y.-T. Chen, S. Wimmer, M. Althammer, T. Wimmer, R. Schlitz, S. Geprägs, H. Huebl, D. Ködderitzsch, H. Ebert, G. E. W. Bauer, R. Gross, and S. T. B. Goennenwein, Observation of the spin Nernst effect, *Nat. Mater.* **16**, 977 (2017).
- [23] T. Miyasato, N. Abe, T. Fujii, A. Asamitsu, S. Onoda, Y. Onose, N. Nagaosa, and Y. Tokura, Crossover Behavior of the Anomalous Hall Effect and Anomalous Nernst Effect in Itinerant Ferromagnets, *Phys. Rev. Lett.* **99**, 086602 (2007).
- [24] C. O. Avci, E. Rosenberg, M. Huang, J. Bauer, C. A. Ross, and G. S. D. Beach, Nonlocal Detection of Out-Of-Plane Magnetization in a Magnetic Insulator by Thermal Spin Drag, *Phys. Rev. Lett.* **124**, 027701 (2020).
- [25] Q. Shao, C. Tang, G. Yu, A. Navabi, H. Wu, C. He, J. Li, P. Upadhyaya, P. Zhang, S. A. Razavi, Q. L. He, Y. Liu, P. Yang,

- S. K. Kim, C. Zheng, Y. Liu, L. Pan, R. K. Lake, X. Han, Y. Tserkovnyak, J. Shi, and K. L. Wang, Role of dimensional crossover on spin-orbit torque efficiency in magnetic insulator thin films, *Nat. Commun.* **9**, 3612 (2018).
- [26] S. Ding, A. Ross, R. Lebrun, S. Becker, K. Lee, I. Boventer, S. Das, Y. Kurokawa, S. Gupta, J. Yang, G. Jakob, and M. Kläui, Interfacial Dzyaloshinskii-Moriya interaction and chiral magnetic textures in a ferrimagnetic insulator, *Phys. Rev. B* **100**, 100406(R) (2019).
- [27] C. O. Avci, A. Quindeau, C. Pai, M. Mann, L. Caretta, A. S. Tang, M. C. Onbasli, C. A. Ross, and G. S. D. Beach, Current-induced switching in a magnetic insulator, *Nat. Mater.* **16**, 309 (2017).
- [28] H. Nakayama, M. Althammer, Y.-T. Chen, K. Uchida, Y. Kajiwara, D. Kikuchi, T. Ohtani, S. Geprägs, M. Opel, S. Takahashi, R. Gross, G. E. W. Bauer, S. T. B. Goennenwein, and E. Saitoh, Spin Hall Magnetoresistance Induced by a Non-Equilibrium Proximity Effect, *Phys. Rev. Lett.* **110**, 206601 (2013).
- [29] S. Vélez, V. N. Golovach, J. M. Gomez-Perez, A. Chuvilin, C. T. Bui, F. Rivadulla, L. E. Hueso, F. S. Bergeret, and F. Casanova, Spin Hall magnetoresistance in a low-dimensional Heisenberg ferromagnet, *Phys. Rev. B* **100**, 180401(R) (2019).
- [30] J. Shan, L. J. Cornelissen, N. Vlietstra, J. Ben Youssef, T. Kuschel, R. A. Duine, and B. J. van Wees, Influence of yttrium iron garnet thickness and heater opacity on the nonlocal transport of electrically and thermally excited magnons, *Phys. Rev. B* **94**, 174437 (2016).
- [31] K. An, R. Kohno, N. Thiery, D. Reitz, L. Vila, V. V. Naletov, N. Beaulieu, J. Ben Youssef, G. De Loubens, Y. Tserkovnyak, and O. Klein, Short-range thermal magnon diffusion in magnetic garnet, *Phys. Rev. B* **103**, 174432 (2021).
- [32] J. S. Jamison, Z. Yang, B. L. Giles, J. T. Brangham, G. Wu, P. C. Hammel, F. Yang, and R. C. Myers, Long lifetime of thermally excited magnons in bulk yttrium iron garnet, *Phys. Rev. B* **100**, 134402 (2019).
- [33] J. Gückelhorn, T. Wimmer, M. Müller, S. Geprägs, H. Hübl, R. Gross, and M. Althammer, Magnon transport in Y3Fe5O12/Pt nanostructures with reduced effective magnetization, *Phys. Rev. B* **104**, L180410 (2021).
- [34] N. Thiery, A. Draveny, V. V. Naletov, L. Vila, J. P. Attané, C. Beigné, G. De Loubens, M. Viret, N. Beaulieu, J. Ben Youssef, V. E. Demidov, S. O. Demokritov, A. N. Slavin, V. S. Tiberkevich, A. Anane, P. Bortolotti, V. Cros, and O. Klein, Nonlinear spin conductance of yttrium iron garnet thin films driven by large spin-orbit torque, *Phys. Rev. B* **97**, 060409(R) (2018).
- [35] L. Sheng, Y. Liu, J. Chen, H. Wang, J. Zhang, M. Chen, J. Ma, C. Liu, S. Tu, C.-W. Nan, and H. Yu, Spin wave propagation in a ferrimagnetic thin film with perpendicular magnetic anisotropy, *Appl. Phys. Lett.* **117**, 232407 (2020).
- [36] J. Shan, P. Bougiatioti, L. Liang, G. Reiss, T. Kuschel, and B. J. Van Wees, Nonlocal magnon spin transport in NiFe₂O₄ thin films, *Appl. Phys. Lett.* **110**, 132406 (2017).
- [37] J. Shan, A. V. Singh, L. Liang, L. J. Cornelissen, Z. Galazka, A. Gupta, B. J. Van Wees, and T. Kuschel, Enhanced magnon spin transport in NiFe₂O₄ thin films on a lattice-matched substrate, *Appl. Phys. Lett.* **113**, 162403 (2018).
- [38] S. Crossley, A. Quindeau, A. G. Swartz, E. R. Rosenberg, L. Beran, C. O. Avci, Y. Hikita, C. A. Ross, and H. Y. Hwang, Ferromagnetic resonance of perpendicularly magnetized Tm₃Fe₅O₁₂/Pt heterostructures, *Appl. Phys. Lett.* **115**, 172402 (2019).
- [39] G. L. S. Vilela, J. E. Abrao, E. Santos, Y. Yao, J. B. S. Mendes, R. L. Rodríguez-Suárez, S. M. Rezende, W. Han, A. Azevedo, and J. S. Moodera, Magnon-mediated spin currents in Tm₃Fe₅O₁₂/Pt with perpendicular magnetic anisotropy, *Appl. Phys. Lett.* **117**, 122412 (2020).
- [40] C. Vittoria, S. D. Yoon, and A. Widom, Relaxation mechanism for ordered magnetic materials, *Phys. Rev. B* **81**, 014412 (2010).
- [41] P. R. Elliston and G. J. Troup, Some antiferromagnetic resonance measurements in α -Fe₂O₃, *J. Phys. C: Solid State Phys.* **1**, 169 (1968).
- [42] Y. Sun, H. Chang, M. Kabatek, Y.-Y. Song, Z. Wang, M. Jantz, W. Schneider, M. Wu, E. Montoya, B. Kardasz, B. Heinrich, S. G. E. te Velthuis, H. Schultheiss, and A. Hoffmann, Damping in Yttrium Iron Garnet Nanoscale Films Capped by Platinum, *Phys. Rev. Lett.* **111**, 106601 (2013).
- [43] C. Hauser, T. Richter, N. Homonnay, C. Eisenschmidt, M. Qaid, H. Deniz, D. Hesse, M. Sawicki, S. G. Ebbinghaus, and G. Schmidt, Yttrium iron garnet thin films with very low damping obtained by recrystallization of amorphous material, *Sci. Rep.* **6**, 20827 (2016).
- [44] R. Schlitz, S. Vélez, A. Kamra, C.-H. Lambert, M. Lammel, S. T. B. Goennenwein, and P. Gambardella, Control of Nonlocal Magnon Spin Transport via Magnon Drift Currents, *Phys. Rev. Lett.* **126**, 257201 (2021).
- [45] T. Wimmer, M. Althammer, L. Liensberger, N. Vlietstra, S. Geprägs, M. Weiler, R. Gross, and H. Huebl, Spin Transport in a Magnetic Insulator with Zero Effective Damping, *Phys. Rev. Lett.* **123**, 257201 (2019).
- [46] H. Jin, S. R. Boona, Z. Yang, R. C. Myers, and J. P. Heremans, Effect of the magnon dispersion on the longitudinal spin Seebeck effect in yttrium iron garnets, *Phys. Rev. B* **92**, 054436 (2015).
- [47] T. Kikkawa, K.-I. Uchida, S. Daimon, Z. Qiu, Y. Shiomi, and E. Saitoh, Critical suppression of spin Seebeck effect by magnetic fields, *Phys. Rev. B* **92**, 064413 (2015).
- [48] B. Flebus, K. Shen, T. Kikkawa, K.-I. Uchida, Z. Qiu, E. Saitoh, R. A. Duine, and G. E. W. Bauer, Magnon-polaron transport in magnetic insulators, *Phys. Rev. B* **95**, 144420 (2017).
- [49] A. Capua, S.-H. Yang, T. Phung, and S. S. P. Parkin, Determination of intrinsic damping of perpendicularly magnetized ultrathin films from time-resolved precessional magnetization measurements, *Phys. Rev. B* **92**, 224402 (2015).
- [50] B. Hillebrands and A. Thiaville, *Spin Dynamics in Confined Magnetic Structures III* (Springer, Berlin, 2006).
- [51] W. Yuan, Q. Zhu, T. Su, Y. Yao, W. Xing, Y. Chen, Y. Ma, X. Lin, J. Shi, R. Shindou, X. C. Xie, and W. Han, Experimental signatures of spin superfluid ground state in canted antiferromagnet Cr₂O₃ via nonlocal spin transport, *Sci. Adv.* **4**, eaat1098 (2018).
- [52] W. Xing, L. Qiu, X. Wang, Y. Yao, Y. Ma, R. Cai, S. Jia, X. C. Xie, and W. Han, Magnon Transport in Quasi-Two-Dimensional van der Waals Antiferromagnets, *Phys. Rev. X* **9**, 011026 (2019).

- [53] S. Y. Huang, X. Fan, D. Qu, Y. P. Chen, W. G. Wang, J. Wu, T. Y. Chen, J. Q. Xiao, and C. L. Chien, Transport Magnetic Proximity Effects in Platinum, *Phys. Rev. Lett.* **109**, 107204 (2012).
- [54] L. J. Cornelissen, J. Liu, B. J. Van Wees, and R. A. Duine, Spin-Current-Controlled Modulation of the Magnon Spin Conductance in a Three-Terminal Magnon Transistor, *Phys. Rev. Lett.* **120**, 097702 (2018).
- [55] J. Liu, L. J. Cornelissen, J. Shan, T. Kuschel, and B. J. Van Wees, Magnon planar Hall effect and anisotropic magnetoresistance in a magnetic insulator, *Phys. Rev. B* **95**, 140402(R) (2017).
- [56] M. Althammer, S. Meyer, H. Nakayama, M. Schreier, S. Altmannshofer, M. Weiler, H. Huebl, S. Geprägs, M. Opel, R. Gross, D. Meier, C. Klewe, T. Kuschel, J.-M. Schmalhorst, G. Reiss, L. Shen, A. Gupta, Y.-T. Chen, G. E. W. Bauer, E. Saitoh, and S. T. B. Goennenwein, Quantitative study of the spin Hall magnetoresistance in ferromagnetic insulator/normal metal hybrids, *Phys. Rev. B* **87**, 224401 (2013).
- [57] T. Kosub, S. Vélez, J. M. Gomez-Perez, L. E. Hueso, J. Faßbender, F. Casanova, and D. Makarov, Anomalous Hall-like transverse magnetoresistance in Au thin films on $Y_3Fe_5O_{12}$, *Appl. Phys. Lett.* **113**, 222409 (2018).
- [58] S. L. Yin, Q. Mao, Q. Y. Meng, D. Li, and H. W. Zhao, Hybrid anomalous and planar Nernst effect in permalloy thin films, *Phys. Rev. B* **88**, 064410 (2013).
- [59] Y.-T. Chen, S. Takahashi, H. Nakayama, M. Althammer, S. T. B. Goennenwein, E. Saitoh, and G. E. W. Bauer, Theory of spin Hall magnetoresistance, *Phys. Rev. B* **87**, 144411 (2013).
- [60] M. Isasa, S. Vélez, E. Sagasta, A. Bedoya-Pinto, N. Dix, F. Sánchez, L. E. Hueso, J. Fontcuberta, and F. Casanova, Spin Hall Magnetoresistance as a Probe for Surface Magnetization in Pt/CoF₂O₄ Bilayers, *Phys. Rev. Appl.* **6**, 034007 (2016).
- [61] L. Baldrati, A. Ross, T. Niizeki, C. Schneider, R. Ramos, J. Cramer, O. Gomonay, M. Filianina, T. Savchenko, D. Heinze, A. Kleibert, E. Saitoh, J. Sinova, and M. Kläui, Full angular dependence of the spin Hall and ordinary magnetoresistance in epitaxial antiferromagnetic NiO(001)/Pt thin films, *Phys. Rev. B* **98**, 024422 (2018).
- [62] S. Geprägs, S. Meyer, S. Altmannshofer, M. Opel, F. Wilhelm, A. Rogalev, R. Gross, and S. T. B. Goennenwein, Investigation of induced Pt magnetic polarization in Pt/Y₃Fe₅O₁₂ bilayers, *Appl. Phys. Lett.* **101**, 262407 (2012).
- [63] Y. M. Lu, J. W. Cai, S. Y. Huang, D. Qu, B. F. Miao, and C. L. Chien, Hybrid magnetoresistance in the proximity of a ferromagnet, *Phys. Rev. B* **87**, 220409(R) (2013).
- [64] B. F. Miao, S. Y. Huang, D. Qu, and C. L. Chien, Physical Origins of the New Magnetoresistance in Pt/YIG, *Phys. Rev. Lett.* **112**, 236601 (2014).
- [65] S. Vélez, V. N. Golovach, A. Bedoya-Pinto, M. Isasa, E. Sagasta, M. Abadia, C. Rogero, L. E. Hueso, F. S. Bergeret, and F. Casanova, Hanle Magnetoresistance in Thin Metal Films with Strong Spin-Orbit Coupling, *Phys. Rev. Lett.* **116**, 016603 (2016).